RADIATION RESEARCH **166**, 544–555 (2006)
0033-7587/06 $15.00

Analytical Functions to Predict Cosmic-Ray Neutron Spectra in the Atmosphere

Tatsuhiko Sato[a,1] and Koji Niita[b]

[a] *Japan Atomic Energy Agency (JAEA) and* [b] *Research Organization for Information Science and Technology (RIST), Ibaraki, Japan*

Sato, T. and Niita, K. Analytical Functions to Predict Cosmic-Ray Neutron Spectra in the Atmosphere. *Radiat. Res.* 166, 544–555 (2006).

Estimation of cosmic-ray neutron spectra in the atmosphere has been an essential issue in the evaluation of the aircrew doses and the soft-error rates of semiconductor devices. We therefore performed Monte Carlo simulations for estimating neutron spectra using the PHITS code in adopting the nuclear data library JENDL-High-Energy file. Excellent agreements were observed between the calculated and measured spectra for a wide altitude range even at the ground level. Based on a comprehensive analysis of the simulation results, we propose analytical functions that can predict the cosmic-ray neutron spectra for any location in the atmosphere at altitudes below 20 km, considering the influences of local geometries such as ground and aircraft on the spectra. The accuracy of the analytical functions was well verified by various experimental data.

INTRODUCTION

In the last decade, protection for aircrews against terrestrial cosmic rays has been one of the most extensively discussed issues in dosimetry. Furthermore, increasing attention has been paid to the soft errors of semiconductor devices induced by the cosmic rays even at the ground level, since the miniaturization of the devices causes a large decrease in their critical charges. These radiation effects are triggered predominantly by neutrons produced by nuclear reactions between the cosmic rays and atmospheric components. Therefore, estimation of cosmic-ray neutron spectra in the atmosphere is an essential issue in the evaluation of the aircrew doses and the soft-error rates (SERs).

A number of studies have been devoted to the estimation of neutron spectra. For instance, Ziegler (*1*) proposed an empirical formula for predicting the high-energy neutron spectra to estimate SERs at ground level. O'Brien *et al.* (*2*) developed a deterministic code LUIN based on an analytical two-component solution of the Boltzmann transport equation. The code is capable of estimating the altitude dependences of aircrew doses and integrated neutron fluxes precisely and is adopted in the route dose calculation code CARI-6 (*3*). Several authors (*4–6*) adopted a Monte Carlo particle transport code, FLUKA (*7, 8*), for the calculation of the cosmic-ray propagation in the atmosphere. Their calculation methods were successful in reproducing the neutron spectra measured at high altitudes, and a similar model was employed in the European Program Package for the Calculation of Aviation Route Doses, EPCARD (*9*). However, the cosmic-ray neutron spectra depend not only on the atmospheric depth, cut-off rigidity and solar modulation (referred to here as global conditions) but also on the structure of the aircraft (*10*) and the water density around the point of interest (*4*) (referred to here as local geometries) in an intricate manner, and none of the existing models can reproduce the measured neutron spectra at any location and time with satisfactory accuracy.

With these situations in mind, we have calculated the cosmic-ray neutron spectra by performing a Monte Carlo particle transport simulation in the atmosphere based on the Particle and Heavy Ion Transport code System, PHITS (*11*), using the latest version of the nuclear data library JENDL-High-Energy File (JENDL/HE) (*12, 13*). In the simulation, cosmic rays with charges up to 28 (Ni) were incident on the Earth system represented by the concentric spherical shells, and the neutron spectra in each shell, i.e. a certain altitude range, were obtained. Based on a comprehensive analysis of the simulation results, we proposed analytical functions to predict the cosmic-ray neutron spectra at any global condition at altitudes below 20 km, considering the local geometry effect.

This paper describes the details of the simulation procedure, together with the comparison of results between the calculated and experimental neutron spectra. The derivation and verification of the analytical function are also discussed in detail below.

MONTE CARLO SIMULATION

Incident Cosmic Rays

In the simulation, cosmic rays were incident on the Earth system at the altitude of 86 km up to which the US-Stan-

[1] Address for correspondence: Research Group for Radiation Protection, Division of Environment and Radiation Sciences, Nuclear Science and Engineering Directorate, Japan Atomic Energy Agency, Tokai, Naka, Ibaraki, 319-1195, Japan; e-mail: sato.tatsuhiko@jaea.go.jp.

dard-Atmosphere-1976 has atmospheric data. Protons, α particles and heavy ions with charges up to 28 (Ni) were considered as the source particles, although the contributions of heavy ions to the cosmic-ray neutron spectra are generally small.

The spectra of the incident particles were estimated by the CREME96 code (*14*). In the code, the effect of the geomagnetic field on the spectra was considered by specifying the McIlwain *L,* where the vertical cut-off rigidity r_c in units of GV is related to this parameter by the simple formula

$$r_c = 14.5/L^2. \quad (1)$$

It should be noted that the output fluxes of CREME96 are the averaged values for all directions after accounting for the solid Earth's shadowing effect. Hence the values should be converted into downward fluxes by multiplying the factor of $4\pi/(4\pi - \Omega_E)$, where Ω_E is the solid angle of the Earth from a point at the altitude of 86 km, to be employed in our simulation.

Atmospheric Propagation

The atmospheric propagation of the incident cosmic rays and their associated cascades was simulated by the PHITS code, which can deal with the transports of all kinds of hadrons and heavy ions with energies up to 200 GeV/nucleon. PHITS is based on the high-energy hadron transport code NMTC/JAM (*15*) and incorporates the MCNP4C code (*16*) for low-energy neutron transports and the JAERI Quantum Molecular Dynamics (JQMD) model (*17*) for simulating nucleus-nucleus interactions. PHITS can also treat the transport of photons, electrons and muons, but they were not considered in our current simulation, since our primary interest was in the evaluation of the neutron spectrum, in which they play a negligible role. Note that such electromagnetic radiations have a significant contribution to the total aircrew dose, and a simulation to estimate their spectra in aircraft is to be performed in the future.

For nuclear reactions induced by neutrons and protons below 3 GeV, the latest version of JENDL/HE was adopted in our simulation instead of the widely used model of the intranuclear cascade (INC) (*18*). This is because the INC model tends to overestimate the yields of high-energy secondary particles knocked out from light nuclei such as nitrogen and oxygen, which are the dominant components of the atmosphere. This tendency causes the overprediction of neutron fluences in deep-penetration calculations.

The atmosphere was divided into 28 concentric spherical shells. The densities and temperatures of each shell were determined referring to the US-Standard-Atmosphere-1976. The atmosphere is assumed to be composed of 75.4% nitrogen, 23.3% oxygen and 1.3% argon by mass above the altitude of 2 km, and additionally, 0.06% hydrogen by mass below this altitude due to the existence of water vapor. Note that argon was replaced by the atom with the same mass number—calcium—in our simulation, since JENDL/HE does not yet include the data for argon. The Earth was represented as a sphere with the radius of 6378.14 km, and its composition was assumed to be 59.2% oxygen, 28.0% silicon, 10.6% aluminum and 2.2% hydrogen by mass. This constitution corresponds to 60% SiO_2, 20% Al_2O_3 and 20% H_2O by mass. The particles arriving at 1000 g/cm^2 below the ground level were discarded in the simulation for reducing the computational time, since there are few albedo neutrons from so deep underground to the atmosphere.

Comparison with Experiments

Figure 1 shows the comparisons of the calculated neutron spectra with the corresponding experimental data obtained by Goldhagen *et al.* (*19*) and Nakamura *et al.* (*20*). Note that all the neutron spectra are expressed in terms of per unit lethargy throughout this paper. The statistical errors in the values obtained by the simulation are generally small—less than approximately 5% and 20% for the high-altitude and ground-level data, respectively, except for very high and low energies. The results at the altitudes below 2 m (~1035 g/cm^2) are depicted in the figure at the ground level to consider the effect of the Earth's albedo neutrons precisely. The spectra predicted by the analytical functions proposed in the next section are also plotted in the figures.

Two peaks around 1 MeV and 100 MeV can be observed in every spectrum. The former is attributed to neutrons emitted by the evaporation process, while the latter is attributed to those produced by the pre-equilibrium and intranuclear cascade processes; these are called the evaporation and the pre-equilibrium peak, respectively, in this paper. The peaks at the thermal energy can be found only in the spectra at the ground level, since they are composed predominantly of the Earth's albedo neutrons.

It is evident from the figure that our simulation can reproduce the experimental data for a variety of global conditions very well. We therefore concluded that the cosmic-ray neutron spectra estimated by our simulation are precise enough to be used in systematic analysis for developing analytical functions. It should be noted that slight overestimations by the simulation can be observed in the evaporation peaks at high altitudes. This discrepancy is due to our ignorance of the shielding effect of aircraft in the spectra; the details of the effect will be discussed in the next section.

ANALYTICAL FUNCTION

Global Condition Dependence of Cosmic-Ray Neutron Spectrum

To analyze the dependences of the cosmic-ray neutron spectra on the global conditions, the simulations of the atmospheric propagation in semi-infinite atmosphere were performed to obtain reference spectra without the disturbance of the local geometry effects. The semi-infinite at-

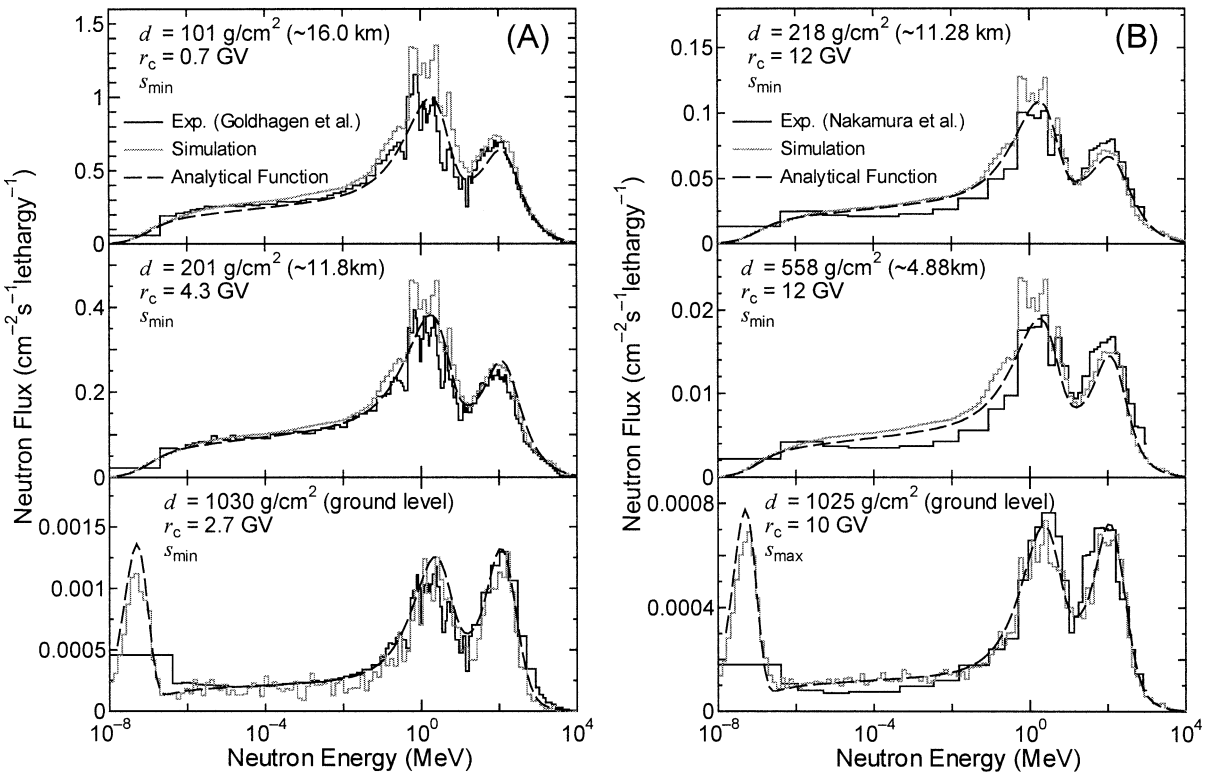

FIG. 1. Calculated and experimental neutron spectra in the atmosphere for various global conditions. Panels A and B show the comparison with the data measured by Goldhagen *et al.* (*19*) and Nakamura *et al.* (*20*), respectively. The values of d and r_c are the atmospheric depth and the cut-off rigidity, respectively, while s_{min} and s_{max} indicate the solar minimum and maximum, respectively. These denotations are also used in the other figures. Equations (10) and (18) were adopted in the calculation of the analytical values for the ground level and high altitudes, respectively.

mosphere consists of the dry air only, even at subterranean regions down to 1000 g/cm² below sea level. The simulations were carried out for the solar minimum and solar maximum with modulation potentials of approximately 465 and 1700 MV, respectively, and 15 geomagnetic fields with the vertical cut-off rigidities from 0.1 to 14 GV.

Figure 2 provides graphical presentations of the global condition dependences of the neutron spectra in the semi-

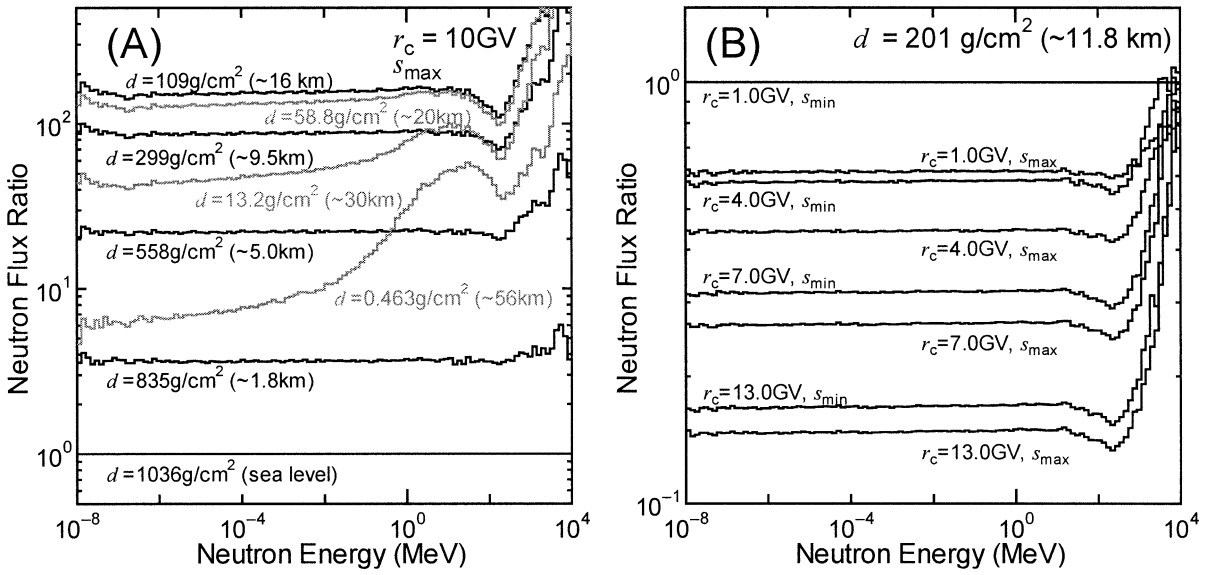

FIG. 2. Neutron flux ratios normalized at (panel A) sea level and (panel B) the solar minimum with the cut-off rigidity 1 GV, obtained by the Monte Carlo simulation for the semi-infinite atmosphere. Panel A shows the atmospheric-depth dependence of the neutron spectra, fixing the cut-off rigidity and the solar condition, while panel B depicts spectral dependence on the cut-off rigidity and the solar condition at a conventional commercial flight altitude. The gray lines in panel A indicate the spectra for the altitudes over the Pfotzer maximum.

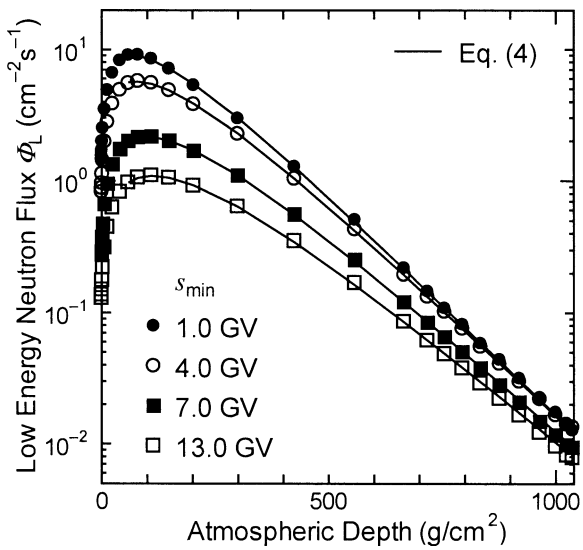

FIG. 3. Integrated fluxes of neutrons with energies below 15 MeV Φ_L under the solar minimum and with several cut-off rigidities.

infinite atmosphere. It is found from the figures that the shapes of the neutron spectra below 15 MeV are almost independent of the global conditions, except for those at the altitudes over Pfotzer maximum (~18 km) as denoted by gray lines in Fig. 2A. This is because equilibrium between production and deceleration of neutrons is established in the lower energy regions. We therefore express the neutron spectra in the semi-infinite atmosphere ϕ_{Inf} as the product of the basic spectrum ϕ_B and the integrated neutron flux below 15 MeV denoted as Φ_L as follows:

$$\phi_{Inf}(s, r_c, d, E) = \phi_B(s, r_c, d, E)\Phi_L(s, r_c, d), \qquad (2)$$

where s, r_c, d and E denote the solar modulation potential, vertical cut-off rigidity, atmospheric depth and neutron energy, respectively; we analyze the dependences of Φ_L and ϕ_B on the parameters separately. The advantage of introducing ϕ_B is that the spectrum below 15 MeV is almost independent of the global conditions for altitudes under 20 km, and it can be expressed by a relatively simple equation, as described later in this section. Since commercial flights never exceed the altitude of 20 km, we will discard the neutron spectra above the altitude in the following analysis for the purpose of simplification and propose analytical functions for predicting the neutron spectra at altitudes under 20 km.

Low-Energy Neutron Flux

The low-energy neutron fluxes Φ_L obtained by the simulations under the solar minimum with several cut-off rigidities are shown in Fig. 3 as a function of the atmospheric depth. As expected from previous studies, Φ_L reaches its maximum at around 100 g/cm^2 and then decreases with the increase in the atmospheric depth. Assuming that the equilibrium between incoming and outgoing low-energy neutrons fluxes is established, the differential equation of Φ_L with respect to the depth can be expressed by

$$\frac{\partial\Phi_L(s, r_c, d)}{\partial d} = N_p(s, r_c, d) - \Sigma_A\Phi_L(s, r_c, d), \qquad (3)$$

where N_P and $\Sigma_A\Phi_L$, respectively, are the number of produced and absorbed neutrons with energies below 15 MeV in the unit volume, with Σ_A denoting the macroscopic absorption cross-section in the atmosphere. The parameter N_P is significantly related to the high-energy particle fluxes, and we assumed that the dependence of N_P on the depth can be represented by an exponential decay curve. Based on the assumption, Φ_L can be expressed by

$$\Phi_L(s, r_c, d) = a_1(s, r_c)\{\exp[-a_2(s, r_c)d] - a_3(s, r_c)\exp[-a_4(s, r_c)d]\}, \qquad (4)$$

where a_1 to a_4 are the parameters depending on the modulation potential and cut-off rigidity. In the derivation of the equation, we also assumed that no neutron exists at the top of the atmosphere, i.e. $\Phi_L(s, r_c, 0) = 0$. If the all assumptions were completely true, then a_3 and a_4 should be equal to 1 and Σ_A, respectively. However, the validity of these assumptions is not always established, and hence a_3 and a_4 are also regarded as the global condition-dependent parameters in our model. The values of the parameters a for each condition were determined by least-squares fitting of the Φ_L data.

Figure 4 plots the parameters obtained as a function of the cut-off rigidity and solar modulation. It is seen from the figure that the differentials of the parameters with respect to the cut-off rigidity generally become the maximum at r_c around 4 GV. The solar modulation affects the parameters only at lower cut-off rigidities except for a_1, since the incident particle spectra calculated by CREME96 are almost independent of the solar condition at higher cut-off rigidities. We therefore introduced a sigmoid function to generate the best-fitting curve to the parameters:

$$a_i(s, r_c) = b_{i1}(s) + \frac{b_{i2}(s)}{1 + \exp[(r_c - b_{i3})/b_{i4}]}, \qquad (5)$$

where b_{i1} to b_{i4} are free parameters, and only b_{11} and b_{i2} are related to the solar modulation; i.e., b_{21}, b_{31}, b_{41}, b_{i3} and b_{i4} are the constant. It should also be noted that the sigmoid function was also adopted in the work of Lewis *et al.* (*21*) for expressing the dependence of aircrew doses on the cut-off rigidity. Table 1 summarizes the numerical values of the parameters b obtained from the least-squares fitting of the a data shown in Fig. 4. We assumed that the dependences of b_{11} and b_{i2} on the solar modulation s can be expressed as a linear relationship:

$$b(s) = \frac{b(s_{min})(s_{max} - s) + b(s_{max})(s - s_{min})}{s_{max} - s_{min}}, \qquad (6)$$

where s_{min} and s_{max} denote the minimum and maximum of s, 465 and 1700 MV, respectively. The validity of the lin-

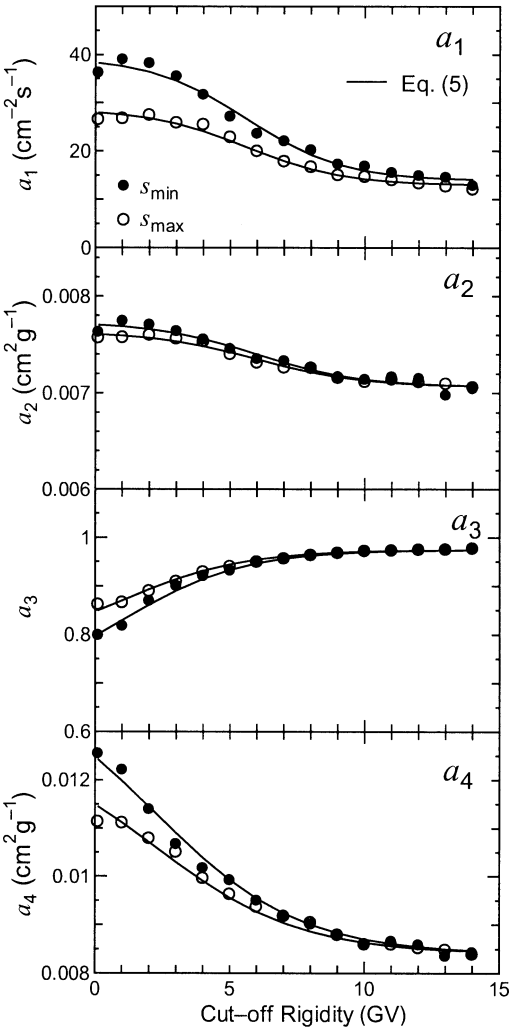

FIG. 4. The dependences of parameters a used in Eq. (4) on the cut-off rigidity. The solid and open circles are the values obtained by the least-squares fitting of the Monte Carlo simulation results for the solar minimum and maximum, respectively, while the solid lines denote the values calculated by the sigmoid function of Eq. (5).

ear-relationship assumption could not be verified, since we performed the Monte Carlo simulation only for the solar minimum and maximum conditions. However, the differences in Φ_L between the two conditions are at most 50%, and the error associated with introducing the assumption can be considered small.

The calculated a parameters using Eq. (5) are also depicted in Fig. 4. The agreements between the data are quite satisfactory for all the cases. The low-energy neutron flux Φ_L can be estimated analytically by substituting the parameters a obtained from Eq. (5) into Eq. (4); the results are also shown in Fig. 3. It is evident from this graph that the analytical function can reproduce the Monte Carlo results very well.

Mean Basic Spectrum

Although the basic spectrum ϕ_B depends on the global conditions, it is worthwhile to analyze the mean basic spectrum $\bar{\phi}_B$ that can be obtained by averaging ϕ_B for all the cases—18 altitude ranges below 20 km, two solar conditions, and 15 geomagnetic fields. The graphical presentation of ϕ_B is given in Fig. 5. To reproduce ϕ_B by an analytical function, we propose the following equation composed of three terms that represent the evaporation and pre-equilibrium peaks, and the pedestal part, respectively:

$$\bar{\phi}_B(E) = c_1\left(\frac{E}{c_2}\right)^{c_3}\exp\left(\frac{-E}{c_2}\right) + c_4\exp\left\{\frac{-[\log_{10}(E) - \log_{10}(c_5)]^2}{2[\log_{10}(c_6)]^2}\right\} + c_7\log_{10}\left(\frac{E}{c_8}\right)\left\{1 + \tanh\left[c_9\log_{10}\left(\frac{E}{c_{10}}\right)\right]\right\} \times \left\{1 - \tanh\left[c_{11}\log_{10}\left(\frac{E}{c_{12}}\right)\right]\right\}, \quad (7)$$

where c_1 to c_{12} are constant parameters. The parameter c_3 is fixed at 0.5 for the conventional evaporation spectrum, but it is regarded as a free parameter in our model since the peak has been disturbed by the deceleration and absorption before the equilibrium is accomplished. Note that

TABLE 1
Numerical Values of the Parameters b used in Eq. (5) Obtained from the Least-Squares Fitting of the a Data Shown in Fig. 4

Unit of a_i	b_{i1}	b_{i2}	b_{i3} (GV)	b_{i4} (GV)
a_1 (cm^{-2} s^{-1})	13.9 (12.9)	25.5 (15.7)	5.62	1.79
a_2 (cm^2 g^{-1})	0.00706	6.73×10^{-4} (5.70×10^{-4})	5.99	1.94
a_3	0.975	0.292 (−0.210)	0.99	2.24
a_4 (cm^2 g^{-1})	0.00840	0.00582 (0.00441)	2.24	2.66

Notes. The values in parentheses are the data for the solar maximum, while the others are those for the solar minimum or the solar-independent parameters. The units of b_{i1} and b_{i2} are the same as those of a_i.

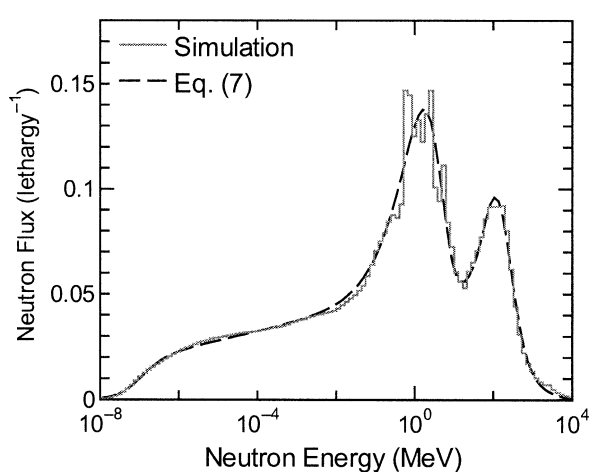

FIG. 5. The mean basic spectrum $\bar{\phi}_B$. The gray line indicates the averaged spectrum for the Monte Carlo results of ϕ_B for all the global conditions except for altitudes over 20 km, while the dashed line denotes the values calculated by Eq. (7).

TABLE 2
Numerical Values of the Parameters c used in Eq. (7) Obtained from the Least-Squares Fitting of the $\bar{\phi}_B$ Data Shown in Fig. 5

Unit of c_i	c_i
c_1 (lethargy^{-1})	0.229
c_2 (MeV)	2.31
c_3	0.721
c_4 (lethargy^{-1})[a]	0.0516
c_5 (MeV)	126
c_6 (MeV)	2.17
c_7 (lethargy^{-1})	0.00108
c_8 (MeV)	3.33×10^{-12}
c_9	1.62
c_{10} (MeV)	9.59×10^{-8}
c_{11}	1.48
c_{12} (MeV)[a]	299

[a] Dependent on the global conditions assumed for estimating ϕ_B.

the second and third terms in the equation were introduced only for reproducing the simulation result, and little physical meaning exists in their forms.

The numerical values of the parameters c obtained from the least-squares fittings of the ϕ_B data shown in Fig. 5 are listed in Table 2. The ϕ_B calculated from Eq. (7) is depicted in Fig. 5. The figure clearly indicates that the analytical function can reproduce the simulation results very well.

Global Condition Dependence of Basic Spectrum

As mentioned before, the basic spectrum ϕ_B depends on the global conditions at energies above 15 MeV. It can be deduced from Fig. 2 that the global conditions affect ϕ_B with regard to the height of the pre-equilibrium peak and the high-energy edge of the spectra. Figure 2B also shows that the influence of the solar condition on ϕ_B is limited to the lower cut-off rigidity cases. We therefore surmised that c_4 and c_{12}, which are respectively related to the magnitude of the pre-equilibrium peak and the high-energy edge of the pedestal part, are dependent on both atmospheric depth and cut-off rigidity, and the others are the constant for all the conditions.

Figure 6 plots the values of c_4 and c_{12} obtained from the least-squares fitting of ϕ_B after fixing the other c parameters for several cut-off rigidities as a function of the atmospheric depth. In general, c_4 rises with an increase in the atmospheric depth and a decrease in the cut-off rigidity, whereas the relation is reversed for c_{12}. For the purpose of estimating the depth dependences of c_4 and c_{12}, we introduced the following functions:

$$c_4(r_c, d) = a_5(r_c) + \frac{a_6 d}{1 + a_7 \exp(a_8 d)} \quad \text{and} \tag{8}$$

$$c_{12}(r_c, d) = a_9(r_c)\{\exp[-a_{10}(r_c)d] + a_{11}(r_c)\exp(-a_{12}d)\}, \tag{9}$$

where a_5 to a_{12} are free parameters, and only a_5, a_9, a_{10} and a_{11} are related to the cut-off rigidity. The numerical values

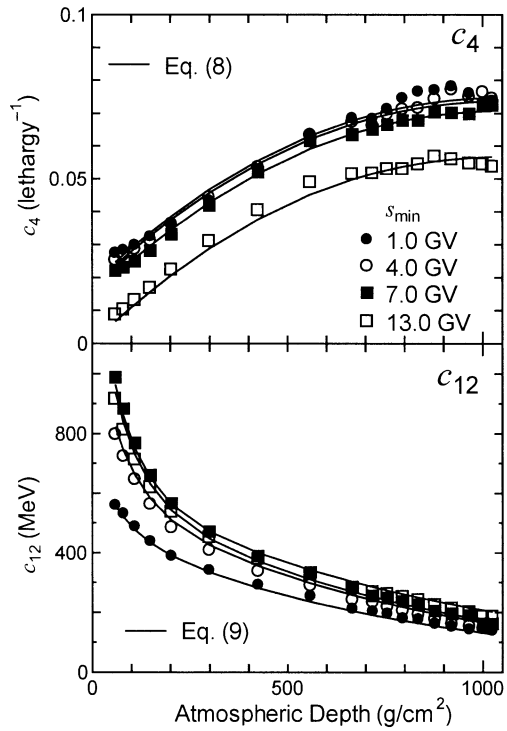

FIG. 6. The parameters c_4 and c_{12} used in Eq. (7) for representing the global-condition dependence of the neutron spectra in the semi-infinite atmosphere.

of the parameters can be obtained by the least-squares fitting of the parameters c_4 and c_{12}. The dependences of a_5, a_9, a_{10} and a_{11} on the cut-off rigidity are illustrated in Fig. 7. For best-fit curves to reproduce the cut-off rigidity dependences of the parameters, we also employed the sigmoid function defined in Eq. (5). Table 3 summarizes the numerical values of the parameters b obtained from the least-squares fitting of the a data shown in Fig. 7, together with the constant values of a_6, a_7, a_8 and a_{12}. The calculated results from the analytical functions adopting these parameters are also shown in Figs. 6 and 7. It is clear from the diagrams that the analytical functions can reproduce the simulation result fairly well.

The basic spectrum ϕ_B for each condition can be estimated using Eq. (7), using the c_4 and c_{12} values obtained from Eqs. (8) and (9), respectively, instead of the data listed in Table 2. The neutron spectra in the semi-infinite atmosphere ϕ_{Inf} can be predicted by multiplying ϕ_B by the low-energy neutron flux Φ_L obtained from Eq. (4), as indicated by Eq. (2).

Comparison with Simulation Results

Figure 8 provides graphical presentations of the comparisons between the neutron spectra in the semi-infinite atmosphere obtained by the simulation and by the analytical function. It is evident from the graphs that the results estimated by the analytical function agree with those by the simulation very well for a variety of global conditions.

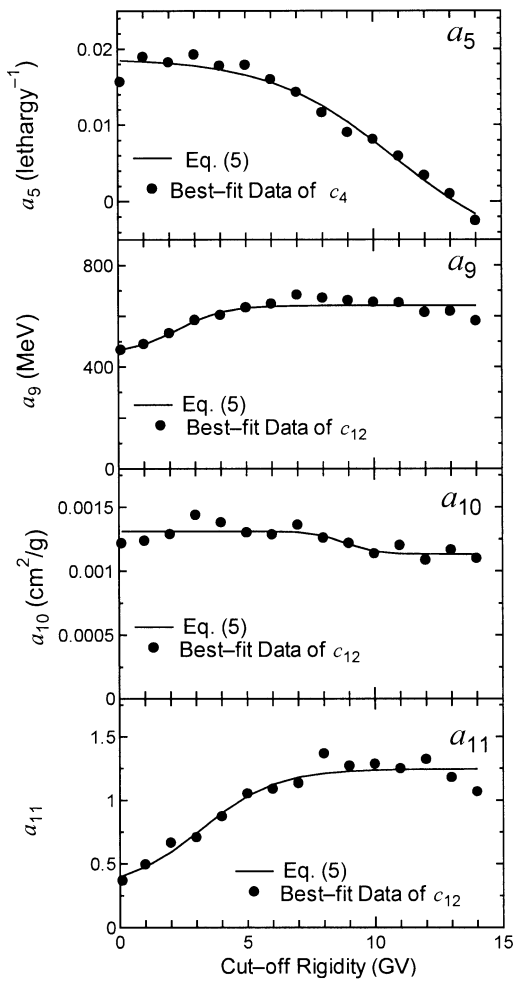

FIG. 7. The dependences of the parameters a used in Eqs. (8) and (9) on the cut-off rigidity.

Equivalent agreements can be observed in the comparisons in other cases, and this enables us to conclude that the analytical function is capable of reproducing the simulation results of the neutron spectra in the semi-infinite atmosphere for any global condition for altitudes under 20 km.

Local Geometry Effect

In practice, the cosmic-ray neutron spectra are different from those in the semi-infinite atmosphere, since they are influenced by the local structures such as the ground conditions, buildings and aircraft. The water density around the point of interest is one of the key quantities in the estimation of spectra at the ground level (*4*), while the configuration of aircraft is of great importance at higher altitudes (*10*). We therefore analyzed the dependences of the neutron spectra on the water density and the aircraft structure as representative of the local geometry effects.

Estimation of Neutron Spectra at Ground Level

To analyze the water-density dependence of the neutron spectra at the ground level, simulations were performed that were similar to those described in the Monte Carlo Simulation section, but with the weight fraction of water, w, in the subterranean region changed from 0 (dry ground) to 1 (pure water). In the simulation, the composition of the rest of the ground is assumed to be 75% SiO_2 and 25% Al_2O_3 by mass; e.g., the ground consists of 60% SiO_2, 20% Al_2O_3 and 20% H_2O by mass for $w = 0.2$, which corresponds to the condition described in the Monte Carlo Simulation section. The neutron spectra for a particular global condition—altitudes below 2 m from the ground level, the solar maximum, and 10 GV cut-off rigidity—were estimated for each ground condition.

Figures 9 and 10 show the absolute and relative values of the neutron spectra compared to the corresponding spectrum in the semi-infinite atmosphere. The figures clearly indicate the significant dependence of the neutron spectra on w especially for lower energies. The low-energy neutron fluxes become larger with the existence of dry ground, since it can be regarded as a reflector of the neutrons. On the other hand, the fluxes decrease with an increase of w, since water works as an absorber of the neutrons. The ground also causes the thermal neutron peak, which cannot be observed in the neutron spectra in the semi-infinite atmosphere.

For the purpose of reproducing the neutron spectra at the ground level ϕ_G by an analytical function, we propose the following equation:

$$\phi_G(s, r_c, d, E, w) = \Phi_L(s, r_c, d)[\phi_B(s, r_c, d, E) f_G(E, w) + \phi_T(E, w)], \quad (10)$$

TABLE 3
Numerical Values of the Parameters a and b used in Eq. (8) and (9) Obtained from the Least-Squares Fittings

Unit of a_i	Function	a_i or b_{i1}	b_{i2}	b_{i3} (GV)	b_{i4} (GV)
a_5 (lethargy^{-1})	Eq. (5)	−0.00701	0.0258	10.9	2.38
a_6 (cm^2 g^{-1} lethargy^{-1})	constant	1.71×10^{-4}			
a_7	constant	0.530			
a_8 (cm^2 g^{-1})	constant	0.00136			
a_9 (MeV)	Eq. (5)	642	−189	2.32	0.897
a_{10} (cm^2 g^{-1})	Eq. (5)	0.00112	1.81×10^{-4}	8.84	0.587
a_{11}	Eq. (5)	1.26	−0.958	3.18	1.47
a_{12} (cm^2 g^{-1})	constant	0.0133			

Note. The units of b_{i1} and b_{i2} are the same as those of a_i.

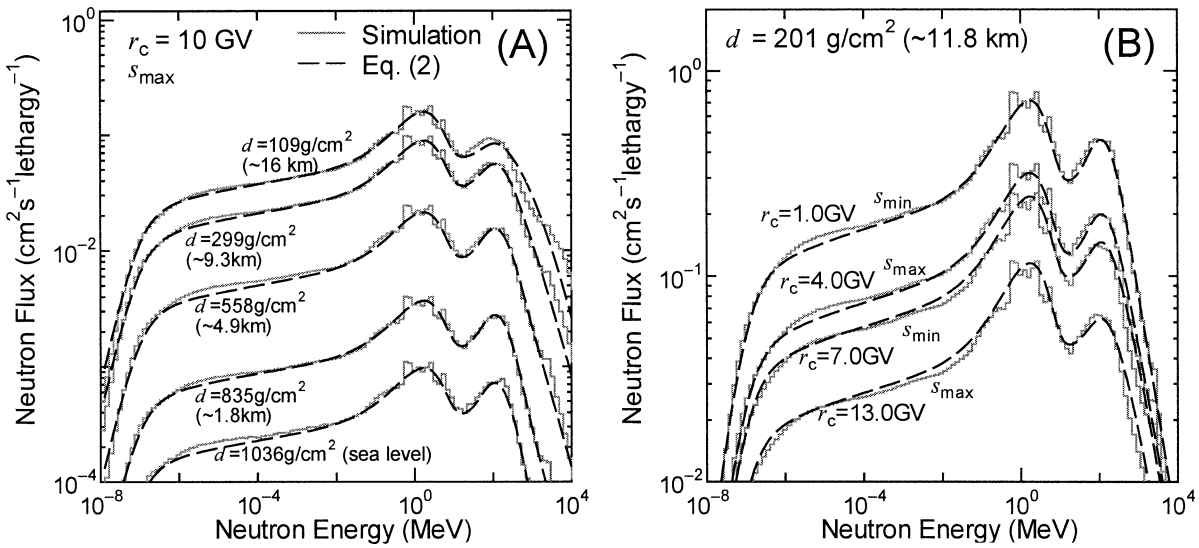

FIG. 8. Calculated neutron spectra in the semi-infinite atmosphere ϕ_{Inf}. Panel A shows the altitude dependence of the neutron spectra, fixing the cut-off rigidity and solar condition, while panel B depicts spectra dependence on the cut-off rigidity and the solar condition at a conventional commercial flight altitude.

where $f_G(E, w)$ denotes the functions representing the disturbance of the spectrum due to the local geometry effect, and $\phi_T(E, w)$ expresses the thermal neutron peak. For neutron energies above 1 eV, ϕ_T becomes negligible and $f_G(E, w)$ corresponds to the value plotted in Fig. 10, i.e., the ratio of neutron flux with the local geometry effect to neutron flux in the semi-infinite atmosphere ϕ_G/ϕ_{Inf}. The reason for taking f_G and ϕ_T to be independent of the global conditions is that the local geometry effect influences these values predominantly in the low-energy region, where the shape of the basic spectrum ϕ_B is independent of the conditions.

We introduced a best-fit curve to the common logarithm of $f_G(E, w)$ as generated by the equation

$$\log_{10}[f_G(E, w)] = g_1 + g_2 \log_{10}\left[\frac{E}{g_3(w)}\right]\left[1 - \tanh\left\{g_4 \log_{10}\left[\frac{E}{g_5(w)}\right]\right\}\right], \quad (11)$$

where g_1 to g_5, are free parameters determined by the least-squares fitting of the ratios of the neutron fluxes shown in Fig. 10. Note that this equation was introduced only for reproducing the simulation results, and little physical meaning was hidden in the form. The numerical values of the parameter g are given in Table 4 except for those of g_3 and g_5. In the fitting, the flux ratios for neutron energies below 1 eV were ignored, since the contributions of thermal neutrons are separately expressed by $\phi_T(E, w)$. The ratios for energies above 500 MeV were also excluded from the fitting because of their poor statistics.

The parameters g_3 and g_5, are related to w, and this dependence is presented graphically in Fig. 11. For the curves

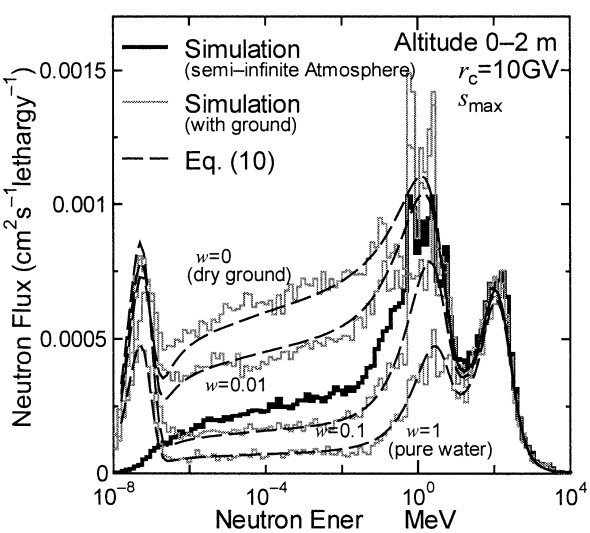

FIG. 9. Calculated neutron spectra at the ground level in comparison with the corresponding spectrum in the semi-infinite atmosphere.

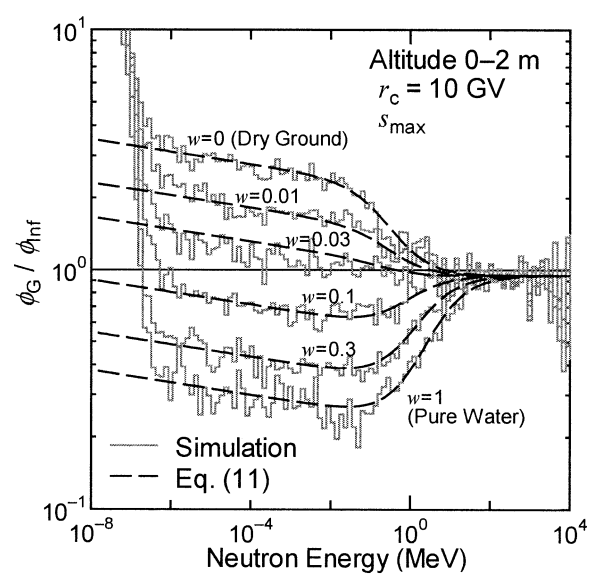

FIG. 10. The ratios of the calculated neutron fluxes at the ground level to the corresponding fluxes in the semi-infinite atmosphere.

TABLE 4
Numerical Values of the Parameters g used in Eqs. (11) and (17) Obtained from the Least-Squares Fittings of the Neutron Flux Ratios shown in Figs. 10 and 12, Respectively

Unit of g_i	g_i	g_{i1}[a]	g_{i2}[b]
g_1	−0.0235	−0.0379	−0.121
g_2	−0.0129	−0.0179	−0.0220
g_3 (MeV)	Eq. (12)	6.03×10^{-8}	5.42×10^{-10}
g_4	0.969	1.36	1.40
g_5 (MeV)	Eq. (13)	5.52	6.45

[a] Location of a pilot.
[b] Location of a cabin passenger.

best fitting g_3 and g_5 respectively, we introduced the function

$$\log_{10}[g_3(w)] = h_{31}\frac{h_{32}}{w + h_{33}} \tag{12}$$

and the third-order polynomial

$$g_5(w) = h_{51} + h_{52}w + h_{53}w^2, \tag{13}$$

respectively, where the parameters h are the fitting constants. Table 5 summarizes the numerical values of the parameters h obtained from the least-squares fitting of the $g(w)$ data shown in Fig. 11, together with those of the constant g parameters. The calculated results of the analytical functions adopting these parameters are also depicted in Figs. 10 and 11. The figures clearly indicate the suitability of the analytical functions for reproducing the simulation results.

The spectrum of the thermal neutron peak can be expressed by

$$\phi_T(E, w) = g_6(w)\left(\frac{E}{E_T}\right)^2 \exp\left(\frac{-E}{E_T}\right), \tag{14}$$

where g_6 denotes the magnitude of the peak and E_T represents the thermal energy. The values of g_6 can be determined by the equation

$$g_6(w) = \frac{\int_0^{1\text{eV}} [\phi_G(s, r_c, d, E, w)/\Phi_L(s, r_c, d) - \phi_B(s, r_c, d, E) f_G(E, w)]\, dE/E}{\int_0^{1\text{eV}} (E/E_T)^2 \exp(-E/E_T)\, dE/E} \tag{15}$$

to reproduce the total flux of thermal neutrons using the analytical functions. The calculated results setting E_T = 0.025 eV are also shown in Fig. 11. Note that the Monte Carlo simulation results were employed for the ϕ_G data in the calculation, while the values obtained from the analytical functions were adopted for Φ_L, ϕ_B and f_G. It is clear from this graph that g_6 generally becomes larger with a decrease of w, probably due to the lower number of thermal neutrons absorbed by water, but the relationship is reversed at the lowest values of w because of a rapid increase of f_G

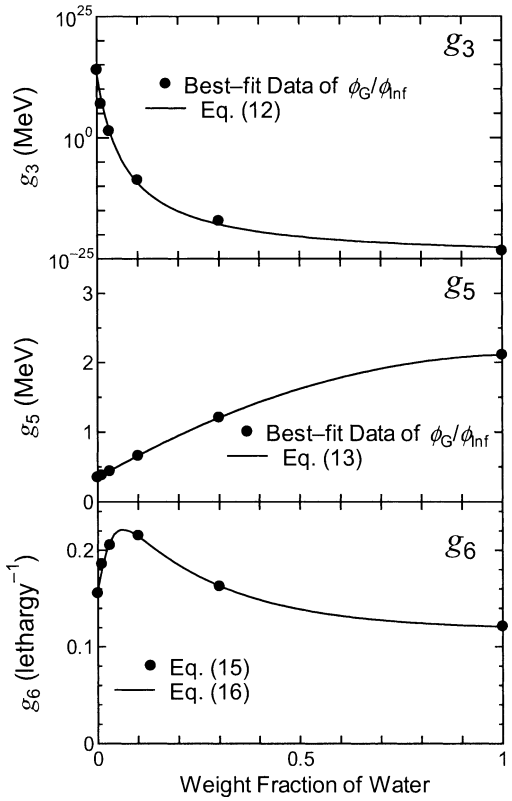

FIG. 11. The dependences of the parameters g used in Eqs. (11) and (14) on the weight fraction of water in the ground.

as shown in Fig. 10. For a best-fit curve to g_6, we introduce the function

$$g_6(w) = \frac{h_{6l} + h_{62}\exp(-h_{63}w)}{1 + h_{64}\exp(-h_{65}w)}, \tag{16}$$

where the parameters h_{6l} are fitting constants determined by the least-squares fitting of the g_6 data. The numerical values of h_{6l} are also given in Table 5, while the graphical fitting result is depicted in Fig. 11.

The neutron spectra at the ground level ϕ_G can be estimated from Eq. (10) by substituting the calculated values of the analytical functions for Φ_L, ϕ_B, f_G and ϕ_T. The results are presented graphically in Fig. 9. The graph indicates that the analytical functions can express the water-density dependence of the neutron spectra satisfactorily. It should be

TABLE 5
Numerical Values of the Parameters h used in Eqs. (12), (13) and (15) Obtained from the Least-Squares Fitting of the $g(w)$ Data Shown in Fig. 11

Unit of g_i	h_{i1}	h_{i2}	h_{i3}	h_{i4}	h_{i5}
g_3 (MeV)	−25.2	2.73	0.0715		
g_5 (MeV)	0.348	3.35	−1.57		
g_6 (lethargy^{-1})	0.118	0.144	3.87	0.653	42.8

Notes. The units of h_{51}, h_{52}, h_{53}, h_{61} and h_{62} are the same as those of the corresponding g parameters. The value of g_3 in unit of MeV can be estimated from Eq. (12) with the given h_{3l} values.

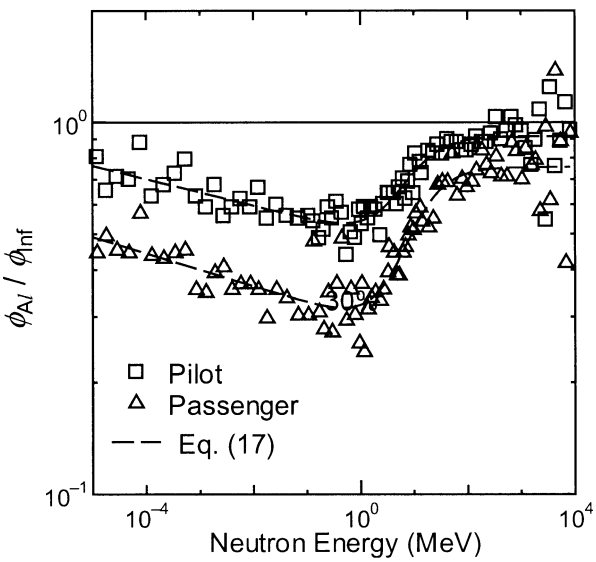

FIG. 12. The ratios of the calculated neutron fluxes inside Airbus-340 at the positions of a pilot and a cabin passenger to those in the free atmosphere. The numerical values denoted by the symbols were calculated from the data shown in figure 4 (A) of ref. (*10*).

noted that not only the weight fraction of water in ground but also the structures of surroundings such as concrete wall and flooring are relevant to the neutron spectra. Furthermore, ground generally consists of a variety of materials with several layers, and hence the assumption of ground with a uniform composition is over simplified for some cases. Therefore, the weight fraction of water used in the functions should be considered not as a purely physical quantity but an adjustable index for representing the existence of various materials, especially for hydrogen, around the point of interest.

Estimation of Neutron Spectra in Aircraft

The influence of aircraft on the neutron spectra was well analyzed by Ferrari *et al.* (*10*). In their work, the particle transport simulations in the mathematical model of Airbus-340 were performed with the FLUKA code, and the neutron spectra at the several locations in the aircraft such as the cockpit and the cabin were estimated. Figure 12 shows the ratios of their calculated neutron spectra inside the aircraft at the positions of a pilot and a cabin passenger to those in the free atmosphere, these data were taken from Figure 4 (A) in their paper (*10*).

A comparison of Figs. 10 and 12 indicates that the aircraft disturbs the neutron spectra in a manner similar to the ground except for the thermal energies. For the function f_{Al} that represents the disturbance of the spectrum due to aircraft, we introduced an equation similar to that describing f_G:

$$\log_{10}[f_{Al}(E, m_A)] = \frac{M_A}{m_{A340}}\left(g_{1l} + g_{2l}\log_{10}\left[\frac{E}{g_{3l}}\right]\left\{1 - \tanh\left[g_{4l}\log_{10}\left(\frac{E}{g_{5l}}\right)\right]\right\}\right), \quad (17)$$

where l indicates the location of interest, i.e. of a pilot or a passenger, g_{1l} to g_{5l} are the fitting constants, and m_A and m_{A340} denote the mass of the aircraft being considered and Airbus-340, respectively. Although the detailed dependence of the spectrum on the aircraft size has not been well investigated, we simply assumed that the common logarithm of f_{Al} was proportional to m_A since the influence of the aircraft structure on the spectrum generally could be expected to become larger with the mass. The values of the parameters g were determined by the least-squares fitting of the data shown in Fig. 12 and by setting $m_A = m_{A340}$. The obtained values were also listed in Table 4, while the calculated results using the parameters are depicted in Fig. 12. It is evident from the graph that the analytical function is capable of reproducing the simulation results well.

The neutron spectra in aircraft ϕ_{Al} can be simply estimated by the equation

$$\phi_{Al}(s, r_c, d, E, m_A) = \Phi_L(s, r_c, d)\phi_B(s, r_c, d, E)f_{Al}(E, m_A). \quad (18)$$

This equation has no term representing the thermal neutron peak, which was considered separately in the estimation of ϕ_G as expressed by Eq. (10). This is justified by the fact that aircraft generally are not large enough to form a thermal neutron peak, as indicated from experimental data (*19, 20*). It should be noted that not only the location and the mass of aircraft but also detailed configuration characteristics, such as the number of passengers and the amount of fuel, affect the neutron spectra, and further studies are desired to develop a more sophisticated model for describing the influence of the aircraft structure on the spectra.

Comparison with Experimental Data

The neutron spectra calculated by Eqs. (10) and (18) for the ground level and high altitudes, respectively, are shown in Fig. 1 for the corresponding global conditions to the experimental data. The weight fraction of water was set at 0.2 for the calculation at the ground level. At high altitudes, the calculations were performed for the pilot location, and the masses of the aircrafts were assumed to be a quarter of m_{A340}, apparently since the airplanes used in their measurements—ER-2 and DC-8—were smaller than Airbus-340.

It is evident from the figures that the neutron spectra of the experiments and the calculations are in excellent agreement. Furthermore, the analytical functions are substantially superior to the Monte Carlo simulation in reproducing experimental data at lower energies, since they can consider the local geometry effect on the spectra even at high altitudes.

The accuracy of the analytical functions was also verified by comparing their calculation results with the experimental data by Kowatari *et al.* (*22*), as shown in Fig. 13. These researchers measured the neutron spectra at the ground level at different altitudes while climbing up Mt. Fuji in Japan. The weight fraction of water w was also set at 0.2 for the analytical calculation. It can be seen clearly from the graph

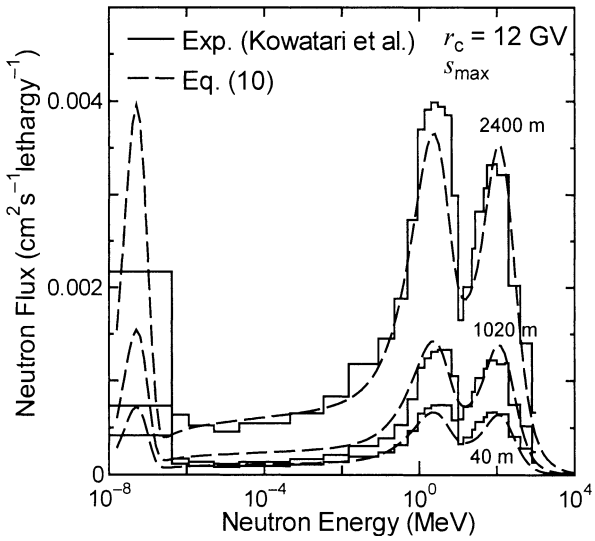

FIG. 13. Neutron spectra calculated with Eq. (10) compared to the measured data in the Mt. Fuji area at the altitudes of 20, 1020 and 2400 m, where the corresponding atmospheric depths are approximately 1030, 915 and 770 g/cm^2, respectively.

that the analytical function can reproduce the experimental data very well. Note that the corresponding Monte Carlo data have not been generated, since it is very time-consuming to perform the simulations with different altitudes of the ground level.

From these considerations, we concluded that our analytical functions can predict cosmic-ray neutron spectra with enough accuracy for any global condition except for altitudes over 20 km, taking the local geometry effects into account.

CONCLUSION

Monte Carlo simulations were performed for estimating the cosmic-ray neutron spectra in the atmosphere by using the PHITS code adopting JENDL/HE. Excellent agreement was observed between the calculated and measured spectra even at the ground level. Based on the comprehensive analysis of the simulation results, we proposed analytical functions that can predict the cosmic-ray neutron spectra for any time and location at the altitudes under 20 km, considering the local geometry effects. The accuracy of the analytical functions was clearly verified by comparing their results with various experimental data.

In the future, the systematic analysis of doses estimated by our analytical functions is needed for their validation in practical use. Further studies are desired to improve the model for describing the local geometry effect on the neutron spectra, since that proposed in this paper incorporates several simplifications. More experimental data for neutron spectra at locations with detailed information on the surrounding structures are required for the purpose, especially for those inside aircraft. Estimation of the photon and charged-particle spectra at high altitudes, also of great importance in aircrew dosimetry, can also be done by applying the Monte Carlo simulation technique established by this work. The simulation technique is also capable of contributing to the estimation of the particle spectra in the atmosphere at solar-geomagnetic storm conditions, an area requiring additional study. Application of this work to the estimation of neutron spectra on the Martian surface will be of great interest in future NASA human space explorations.

ACKNOWLEDGMENTS

We would like to thank Dr. Y. Watanabe and Dr. T. Fukahori for their support in incorporating JENDL/HE into PHITS and Dr. A. Endo, Dr. M. Kowatari, Dr. T. Nunomiya, Dr. H. Yasuda and Dr. T. Nakamura for their advice on this work. We also wish to thank the technical staff of the CCSE office of JAEA for their help in performing the Monte Carlo simulation.

Received: February 28, 2006; accepted: May 11, 2006

REFERENCES

1. J. F. Ziegler, Terrestrial cosmic ray intensities. *IBM J. Res. Dev.* **42**, 117–139 (1998).
2. K. O'Brien, W. Friedberg, H. H. Sauer and D. F. Smart, Atmospheric cosmic rays and solar energetic particles at aircraft altitudes. *Environ. Int.* **22** (Suppl. 1), S9–S44 (1996).
3. W. Friedberg, K. Copeland, F. E. Duke, K. O'Brien and E. B. Darden, Guidelines and technical information provided by the U.S. Federal Aviation Administration to promote radiation safety for air carrier crew members. *Radiat. Prot. Dosim.* **86**, 323–327 (1999).
4. S. Roesler, W. Heinrich and H. Schraube, Calculation of radiation fields in the atmosphere and comparison to experimental data. *Radiat. Res.* **149**, 87–97 (1998).
5. A. Ferrari, M. Pelliccioni and T. Rancati, Calculation of the radiation environment caused by galactic cosmic rays for determining air crew exposure. *Radiat. Prot. Dosim.* **93**, 101–114 (2001).
6. J. M. Clem, G. De Angelis, P. Goldhagen and J. W. Wilson, New calculations of the atmospheric cosmic radiation field–results for neutron spectra. *Radiat. Prot. Dosim.* **110**, 423–428 (2004).
7. A. Fasso, A. Ferrari and P. R. Sala, Electron-photon transport in FLUKA: status. In *Proceedings of the Monte Carlo 2000 Conference,* Lisbon, Oct. 23–26 (A. Kling, F. Barao, M. Nakagawa, L. Tavora and P. Vaz, Eds.), pp. 159–164. Springer-Verlag, Berlin, 2001.
8. A. Fasso, A. Ferrari, J. Ranft and P. R. Sala, FLUKA: status and prospective for hadronic applications. In *Proceedings of the Monte Carlo 2000 Conference,* Lisbon, Oct. 23–26 (A. Kling, F. Barao, M. Nakagawa, L. Tavora and P. Vaz, Eds.), pp. 955–960. Springer-Verlag, Berlin, 2001.
9. H. Schraube, V. Mares, S. Roesler and W. Heinrich, Experimental verification and calculation of aviation route doses. *Radiat. Prot. Dosim.* **86**, 309–315 (1999).
10. A. Ferrari, M. Pelliccioni and R. Villari, Evaluation of the influence of aircraft shielding on the aircrew exposure through an aircraft mathematical model. *Radiat. Prot. Dosim.* **108**, 91–105 (2004).
11. H. Iwase, K. Niita and T. Nakamura, Development of a general-purpose particle and heavy ion transport Monte Carlo code. *J. Nucl. Sci. Technol.* **39**, 1142–1151 (2002).
12. T. Fukahori, Y. Watanabe, N. Yoshizawa, F. Maekawa, S. Meigo, C. Konno, N. Yamano, A. Yu. Konobeyev and S. Chiba, JENDL High Energy File. *J. Nucl. Sci. Technol. Suppl.* **2**, 25–30 (2002).
13. Y. Watanabe, T. Fukahori, K. Kosako, N. Shigyo, T. Murata, N. Yamano, T. Hino, K. Maki, H. Nakashima and S. Chiba, Nuclear data evaluations for JENDL high-energy file. In *Proceedings of Interna-*

tional Conference on Nuclear Data for Science and Technology, pp. 326–331. American Institute of Physics, New York, 2005.

14. A. J. Tylka, J. H. Adams, Jr., P. R. Boberg, B. Brownstein, W. F. Dietrich, E. O. Flueckiger, E. L. Petersen, M. A. Shea, D. F. Smart and E. C. Smith, CREME96: A revision of the cosmic ray effects on micro-electronics code. *IEEE Trans. Nucl. Sci.* **44**, 2150–2160 (1997).

15. K. Niita, S. Meigo, H. Takada and Y. Ikeda, *High Energy Particle Transport Code NMTC/JAM.* JAERI-Data/Code 2001-007, Japan Atomic Energy Research Institute, Ibaraki, 2001.

16. J. F. Briesmeister, *MCNP—A General Monte Carlo n-Particle Transport Code.* LA-12625-M, Los Alamos National Laboratory, Los Alamos, NM, 1997.

17. K. Niita, S. Chiba, T. Maruyama, H. Takada, T. Fukahori, Y. Nakahara and A. Iwamoto, Analysis of the (N,xN′) reactions by quantum molecular dynamics plus statistical decay model. *Phys. Rev.* **C52**, 2620–2635 (1995).

18. H. W. Bertini, Low-energy intranuclear cascade calculation. *Phys. Rev.* **131**, 1801–1821 (1963).

19. P. Goldhagen, J. M. Clem and J. W. Wilson, The energy spectrum of cosmic-ray induced neutrons measured on an airplane over a wide rage of altitude and latitude. *Radiat. Prot. Dosim.* **110**, 387–392 (2004).

20. T. Nakamura, T. Nunomiya, S. Abe, K. Terunuma and H. Suzuki, Sequential measurements of cosmic-ray neutron spectrum and dose rate at sea level in Sendai, Japan. *J. Nucl. Sci. Technol.* **42**, 843–853 (2005).

21. B. J. Lewis, L. G. I. Bennett, A. R. Green, M. J. McCall, B. Ellaschuk, A. Butler and M. Pierre, Galactic and solar radiation exposure to aircrew during a solar cycle. *Radiat. Prot. Dosim.* **102**, 207–227 (2002).

22. M. Kowatari, K. Nagaoka, S. Satoh, Y. Ohta, J. Abukawa, S. Tachimori and T. Nakamura, Evaluation of the altitude variation of the cosmic-ray induced environmental neutrons in the Mt. Fuji area. *J. Nucl. Sci. Technol.* **42**, 495–502 (2005).